

Multiscale Design of Au-Based Alloys for Improved Plasmon Delivery and Nanoheating in Near-Field Transducers

Okan K. Orhan,^{1,2} Frank Daniel Bello,¹ Nicolás Abadía,³ Ortwin Hess,¹ John F. Donegan,¹ and David D. O'Regan¹

¹*School of Physics, SFI AMBER Centre and CRANN Institute,
Trinity College Dublin, The University of Dublin, Dublin 2, Ireland*

²*Department of Mechanical Engineering, University of British Columbia, Vancouver, BC, V6T 1Z4, Canada*

³*School of Physics and Astronomy and Institute for Compound Semiconductors, Cardiff University, Cardiff, CF24 3AA, U.K*

Plasmonic near-field transducers (NFTs) play a key role in administering nanoscale heating for a number of applications ranging from medical devices to next generation data processing technology. We present a novel multi-scale approach, combining quantum many-body perturbation theory with finite-element modelling, to predict the electric and thermal material parameters of various Au-based, noble metal (M) alloys. Specifically, we focus on modelling their performance within an NFT designed to focus high-intensity, sub-diffracted light for technologies such as nanoscale etching, manipulation, sensing, and heat-assisted magnetic recording (HAMR). Elemental Au is the long-standing general-purpose NFT medium due its excellent plasmonic performance at relevant wavelengths. However, elemental Au is a soft, ductile material that tends to extrude and deform in response to extreme temperature gradients. Therefore, alloying Au with other noble metals such as Ag, Cu, Pd or Pt, has attracted considerable interest for improved mechanical and thermal robustness while reaching threshold plasmonic generation at standard optoelectronics operating wavelengths (e.g., ≈ 830 nm) and approximate high-power NFT temperatures (≈ 400 K). We predict that certain Au-Ag alloys may offer improved thermal stability as whole-NFT media compared to elemental Au, alongside plasmonic figures of merit comparable to that of Au. Simulations of certain solid solution Au-Pd/Pt alloys enable us to predict significantly enhanced thermal conductivity. We predict that alloying with Pd at low concentrations $\sim 10\%$ may preserve the NFT performance of Au, while offering the benefits of improved thermal and mechanical stability.

I. INTRODUCTION

Au nano-particles and thin-films are widely used in plasmonic media for opto-electronic applications such as optical and bio-sensing [1–3], light and heat-assisted drug delivery systems [4–6], as well as data processing and recording [7–12]. This is due to their high plasmonic performance throughout the near-infrared-visible (IR-vis) spectral range [13]. However, these applications often operate at temperatures above room temperature, where dephasing rates increase and the thermal conductivity of Au decreases significantly. This can be detrimental for nanoscale components and device operation [14]. It is well known that Au is soft and may protrude or deform regardless of design and given increases in temperature as little as a few tens of Kelvin [15]. These issues greatly reduce the thermal stability and therefore manufacturability of many Au-based nano-devices. Hence, alloying Au with other noble metals such as Ag, Cu, Pd and Pt has been proposed to engineer both plasmonic and thermal properties for designated applications [16–21]. This is true, for example, in heat-assisted magnetic recording (HAMR), where the temperatures of near-field transducers (NFTs) may exceed 400 K [16, 22].

This present work is a proof-of-concept for a multi-scale modelling workflow that goes from beyond-density-functional theory first-principle electronic structure upwards in scale. Using this, we carried out a simulated performance assessment of Au-based alloys as they fully

or partially substitute the metallic components within a metal-insulator-semiconductor (MIS) NFT that was previously designed to be used in the HAMR device, as described in detail in Ref. 9. The approach developed, and the alloys explored, could in principle also be used to improve other NFT designs used in nano-heating applications such as bowtie, E- or C-aperture, as well as a number of nanoparticle designs such as nanoparticle-on-mirror (NPoM) structures, to name a few. Since it is impractical to explore all possible alloy compositions, in what follows in this proof of principle will look at two different alloying regimes, focusing first on evaluating the plasmonic performance of mono-layer-stacked and fully disordered bulk Au-Ag/Cu alloys, followed by that of fully disordered bulk Au-Pd/Pt alloys, throughout their composition space. The multi-scale approach involves calculating first-principles electronic parameters including quasiparticle renormalization effects at the perturbative G_0W_0 level, and on this basis then generating semi-empirical plasmonic and thermal material parameters, which in the final step are fed into finite-element method (FEM) simulations to assess NFT device-level performance of the simulated alloys.

The example NFT design that we use as an example here [9] is from the context of HAMR, a next-generation high-density recording technology expected to store information on a ground-breaking scale of tens of terabytes per square inch [9, 12]. The fundamental principle behind HAMR is the nanosecond-scale heating of a local

region in the recording medium above its Curie temperature using sub-diffraction focused light; and by doing so, the reducing of the coercivity of the region in order to enable magnetic recording. The key component of this operation is the near-field transducer [22, 25] operating as a plasmonic antenna used for local and fast heating. Depending on the NFT, such a task requires either a localized surface-plasmon (LSP) [26, 27], or a symmetric surface plasmon polariton (SPP) [28] mode at the operation wavelength. Regardless of the particular design, the heat-write-cool operation cycle has to be safely repeated many thousands of times for a viable HAMR device. For this, a sufficiently high plasmon population is required to heat the recording medium above its Curie temperature, while avoiding overheating of the metallic tip and accompanying heat sink in NFTs at the operation wavelength, for which we choose 830 nm following Ref. 9.

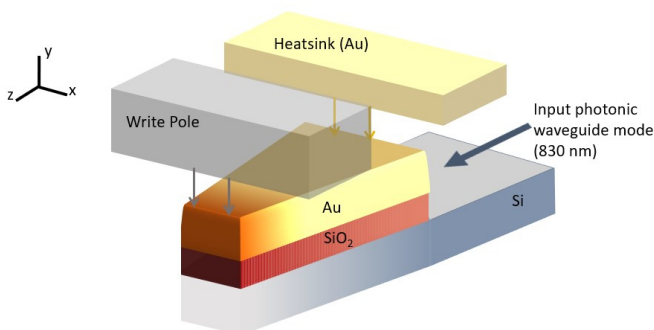


FIG. 1. Schematic diagram of the hybrid antenna-based NFT used in multi-scale simulations, as designed in Ref. 9, demonstrating the placement of the write pole and metallic heat-sink that is composed of Au or an Au alloy. The air-bearing surface (ABS) lies in front of the narrowest tapered region, which sits only a few nanometers above the recording medium. Coupled FEM simulations of Maxwell’s equations along with the heat equation were carried out, [9, 10, 16] with full simulation details provided in the Supplemental Material [30].

The NFT design in question, schematically illustrated in Fig. 1, is a plasmonic antenna designed as a MIS layered structure that supports a SPP in order to produce sub-diffraction focused light, which is then converted to heat within the recording medium. This NFT was designed by Abadía *et al.* for SPP generation at a single mode wavelength of 830 nm, particularly for operation in a HAMR apparatus [9, 31, 32]. For optimal HAMR operation, heating should be confined at a $50 \times 50 \text{ nm}^2$ area or less on the recording medium. This is achieved by using a plasmonic tip as small as 20 nm in the cross-track (x) direction of Fig. 1 [9]. The small size scale combined with the softening tendency of the elemental Au under relatively high temperatures makes the plasmonic tip potentially vulnerable to deformation. Therefore, it would be beneficial if the Au component of the nanostructure can be replaced with alloys that could significantly increase the thermal stability and hardness of the NFT, in

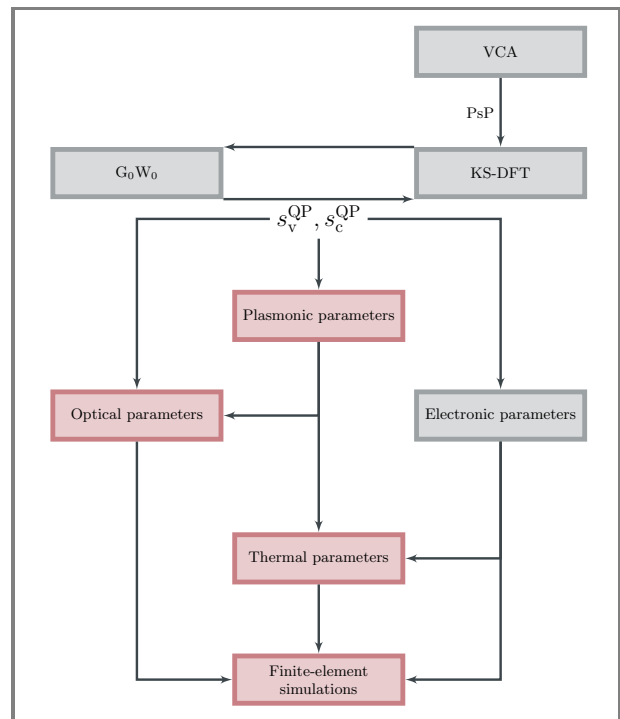


FIG. 2. Schematic illustration of the work-flow followed here to obtain the material parameters for finite-element simulations. The virtual crystal approximation (VCA) is used to model virtual atoms of Au alloys with pseudo-potentials (PsP), which are then fed into the approximate Kohn-Sham density-functional theory (KS-DFT). Band stretching factors (s_v^{QP} and s_c^{QP}) are then obtained by means of linear regression to quasiparticle energies calculated using one-shot non-self-consistent many-body perturbation theory (G_0W_0). Please see Section II for details. Color codes are assigned to the first-principles parameters as gray and the semi-empirical parameters as pink. See the Supplemental Material [30] for full lists of parameters used and details of the computational methodology.

particular at the air-bearing surface [9, 31].

The primary criterion for any NFT design is generating sufficient plasmon populations, particularly high-quality SPPs for this particular design. Two plasmonic figure-of-merits (p-FOMs) are used to assess the quality of SPP generation in this work. The first p-FOM is the electron-energy loss spectrum (EELS) given by [33–39]

$$\text{EELS} = -\Im[1/\mathcal{E}] , \quad (1)$$

where $\mathcal{E} = \mathcal{E}_1 + i\mathcal{E}_2$ is the complex macroscopic dielectric function. EELS checks for a sufficient presence of nearly free electrons available for collective oscillations rather than forming particle-hole pairs at a given wavelength [40]. The second p-FOM is the quality of a generated SPP, indicating its longevity, given by [41]

$$Q_{\text{SPP}}(\omega) = \mathcal{E}_1^2/\mathcal{E}_2. \quad (2)$$

We obtained the macroscopic dielectric function using the procedure defined in Ref. 6 along with thermal pa-

parameters such as thermal conductivity and heat capacity. Furthermore, we extracted the relevant quantities in the cases of ordered Au-Ag and Au-Cu alloys directly from the same work. This method is summarized in Section II and the description of results and optimum Au-alloys for nano-heating is provided in Section III.

II. THEORETICAL SPECTROSCOPY SIMULATIONS

A systematic illustration of the work-flow used to obtain the material parameters needed for the finite-element simulations is shown in Fig. 2. Approximate Kohn-Sham density-functional theory (KS-DFT) [43, 44], which uses local and semi-local approximations for exchange and correlation [44–47], was used for constructing an initial approximation for the band-structure. KS band-structures, in particular, offer convenient starting points for perturbative linear-response theoretical spectroscopy approaches, such as the random-phase approximation (RPA) [37–39, 48]. However, the next accuracy of the RPA is highly dependent on the accuracy of electronic band-structure provided as its starting point, and in particular the dressing of independent particles and holes by excitations can be important. It has been shown that KS-DFT using local-density approximations performs poorly in the case of noble metals [6, 49] due to absent non-local electronic exchange-correlation effects. This error becomes more pronounced in spectral simulations, not least in the case of noble metals [6, 50–54]. This can be partially overcome by providing a quasi-particle band-structure, rather than the non-interacting Kohn-Sham DFT band-structure, as the starting point for RPA. In this work, we applied a set of stretching operators, which were obtained using one-shot, non-self-consistent GW (G_0W_0) [6, 8] from first principles to the KS band-structures. The resulting stretched KS band-structures are used both in spectral simulations and determination of fundamental material parameters such as thermal conductivity (See Supplemental Material [30] for details).

The conventional RPA operates in the product space of the occupied and unoccupied KS wave-functions, and these occupancies need to be defined with high precision. In metals, in order to accurately recover the Drude peak generated by intra-band transitions within the RPA, an unfeasibly dense Brillouin zone sampling of the Fermi surface is required [56]. As a result, and following established practice in this area, in this work the Drude plasmon contribution (also called the intra-band contribution) to the macroscopic dielectric function (\mathcal{E}) is included via the Drude-Lorentz classical model [57–60], where it is given by

$$\mathcal{E}^{\text{intra}}(\omega) = \varepsilon_\infty - \frac{\omega_p^2}{\omega^2 - i\eta_p\omega}. \quad (3)$$

Here, ω_p , η_p , and ε_∞ are the Drude plasmon energy,

the phenomenological inverse life-time, and the electric permittivity at the infinite-frequency limit, respectively. In order to construct a practical multi-scale work-flow appropriate to materials exploration and interpolation, a phenomenological inverse life-time and the electric permittivity are determined from the experimental spectra of the elemental metals in the infra-red region.

For a uniform, non-interacting electron gas, the Drude plasmon energy can be approximated by [57, 58, 61]

$$\omega_p^2 = \frac{4\pi N(E_F)}{m_{\text{eff}}}, \quad (4)$$

where $N(E_F)$ is the density of states (DOS) at the Fermi level and m_{eff} is the electron effective mass. The Drude plasmon energy can, however, be calculated within first principles starting from the electronic band structure using one-band theory [62]. Within the one-band theory, the effective mass of the metallic band is defined by assuming that these bands have a parabolic dispersion to the Fermi surface given by [62],

$$\begin{aligned} m_{\text{eff}}^{-1} &\approx \frac{1}{3} \langle v^2(E_F) \rangle \\ &= \frac{1}{3} \left(\sum_i \int_{S_{F_i}} d\mathbf{k} v_i^2(\mathbf{k}) \right) \left(\sum_j \int_{S_{F_j}} d\mathbf{k}' \right)^{-1}, \\ \text{if } v_i^2(\mathbf{k}) &= \left| \frac{\partial E_{i,\mathbf{k}}}{\partial \mathbf{k}} \right|^2, \end{aligned} \quad (5)$$

where S_{F_i} is the Fermi surface of the i^{th} metallic band. This yields a Drude plasmon energy that can be approximated as

$$\omega_p^2 = \frac{4\pi}{3} N(E_F) \langle v^2(E_F) \rangle. \quad (6)$$

Our work finds that Au-Ag binary alloys form continuous face-centered cubic (FCC) solids for any given stoichiometric ratios, rather than an ordered alloy. This is because they exhibit only short-range ordering [63]. While the Au-Cu alloys also prefer the continuous FCC phase, the Au_3Cu , AuCu , and AuCu_3 shows ordered structures at $\approx 400 - 700$ K [64]. Similarly, Au_3Pd and AuPd_3 at $\approx 900 - 1110$ K, as well as AuPd at $\approx 300 - 400$ K, show ordered structures with the continuous FCC phase being a general trend for other stoichiometric ratios and temperature ranges [65]. In the case of the Au-Pt alloys, there is a large miscibility gap, where Au and Pt forms local sub-structures for $\gtrsim 15\%$ ratio of Pt at the lower temperatures; however, there is still the continuous FCC phase of the low-concentration Pt alloys at ≈ 400 K, and high-concentration Pt alloys exist in a very narrow temperature belt between the miscibility and liquid phase regions of higher temperatures [66]. Hence, most of the Au-M alloys in this work have continuous FCC solid solutions without long-range ordering. The most suitable approach would be getting statistical averaging of every possible spatial configuration within a quite large cell, namely the super-cell approximation,

to be able to include the disorder in such alloys. However, it is not feasible for high-throughput simulations. An expedient approach, instead, is to replace the Au-M atom pairs with a virtual atom, which interpolates the behaviours of original atoms, namely the virtual crystal approximation (VCA) [67, 68]. This can be applied within the approximate KS-DFT via a mixing scheme for the pseudo-potential (PsP) of the virtual atom using the constituting atoms A and B, given by [68]

$$V_{\text{PsP}}^{\text{virtual}}(\mathbf{r}, \mathbf{r}') = (1 - x)V_{\text{PsP}}^{\text{A}}(\mathbf{r}, \mathbf{r}') + xV_{\text{PsP}}^{\text{B}}(\mathbf{r}, \mathbf{r}'). \quad (7)$$

Here, ‘ x ’ refers to the amount of alloyed metal. The VCA provides a simple scheme for fully disordered case, which excludes any ordering, both long-range and short-range.

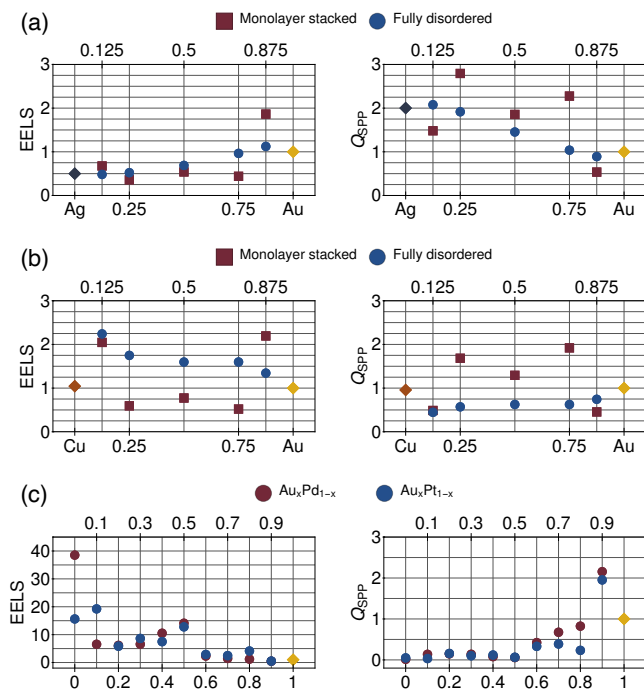


FIG. 3. Amplitudes at 830 nm of electron energy-loss (left column) and the surface-plasmon polariton quality factor (right column) of row (a) the mono-layer-stacked and fully disordered Au-Ag alloys; row (b) mono-layer-stacked and fully disordered Au-Cu alloys, and (c) fully disordered Au-Pd/Pt alloys. All values are normalized against the elemental Au values, which are set to a value of 1. The ordered Au-Ag and Au-Cu alloy cases were extracted from Ref. 6, for which the matching fractional stoichiometric ratios for the fully ordered were chosen.

III. RESULTS

Despite being a well-known plasmonic metal, elemental Ag produces weaker plasmons than Au at 830 nm, indicated by its normalized EELS amplitude in Fig. 3 (a, left), as it has a single and narrow plasmonic peak at ~ 330 nm [6]. However, the small population of SPPs

of Ag-rich alloys is longer lived compared to that of elemental Au, shown in Fig. 3 (a, right). Interestingly, the mono-layer-stacked AuAg₃ exhibits exceptionally high quality SPPs, while still exhibiting significant simulated generation. Furthermore, it has a predicted thermal conductivity of $\kappa = 669$ ($\text{Wm}^{-1}\text{K}^{-1}$), significantly higher than the $\kappa = 312$ ($\text{Wm}^{-1}\text{K}^{-1}$) of the elemental Au. To calculate the conductivity, we included various approximated scattering processes such as the electron-phonon, the electron-electron, as well as the electron-impurity scattering and also subsequently calculated the specific heat capacity for FEM simulations of the heat equation (see Supplemental Material [30] for details and values).

The elemental metals Au and Cu exhibit rather similar affinities for SPP generation. Disordered Au_xCu_{1-x} alloys produce lower quality SPPs, as shown in Fig. 3 (b), regardless of the fractional ratios. On the other hand, mono-layer-stacked Au₃Cu, AuCu, and AuCu₃ show improved qualities in simulation, with strong plasmons as well as improved thermal conductivities compared to both the elemental Au and Cu (see Supplemental Material [30]). As shown in Fig. 3 (c), Pd- and Pt-rich alloys produce strong, but quite short-living plasmons. On the contrary, Au-rich fully disordered Au-Pd/Pt improve the SPP qualities significantly. Unfortunately, mixing Au with either Pd or Pt appears to substantially reduce thermal conductivity, unsurprisingly as the elemental Pd and Pt are relatively poor thermally conductive materials.

We performed FEM simulations using the candidate alloys with promising plasmon generation and improved thermal conductivity. In the NFT design, SPPs are generated by using a 3-fold process, namely; (1) effective index matching, for a photonic waveguide mode with the plasmonic mode, done by adjusting the thickness of the insulator layer, (2) designing the MIS waveguide component as a Fabry-Perot cavity, and (3) tapering to achieve localized heating suitable in media for HAMR. In Fig. 4(b) and 4(c), we show the temperature, heat flux, and thermal gradients of the NFT and within the center of a FePt magnetic layer often used in recording media (see Supplemental Material [30] for full media materials/dimensions). The size of the heated region may be controlled by adjusting the input power. This is vital for maximizing areal bit densities, i.e., cross (x-axis) and down (y) track regions, in magnetic recording devices. The bulk of the power within the NFT is seen to be concentrated within the tip of the NFT (red region) [69]

Table I contains a comparative analysis of the thermal performance [22] when replacing the Au components with various Au alloys as well as the last 10 nm section from the ABS. Figure of merits used to quantify the thermal performance of the NFT are adopted from Refs. 22 and 9. The dimensions of the NFT design used in simulations, being originally optimized using pure Au, are left unchanged. Therefore, we notice comparable optical performance (required input power, P_{in}) using alloys with similar refractive indices to Au. We find that in order to simultaneously have an improved thermal performance,

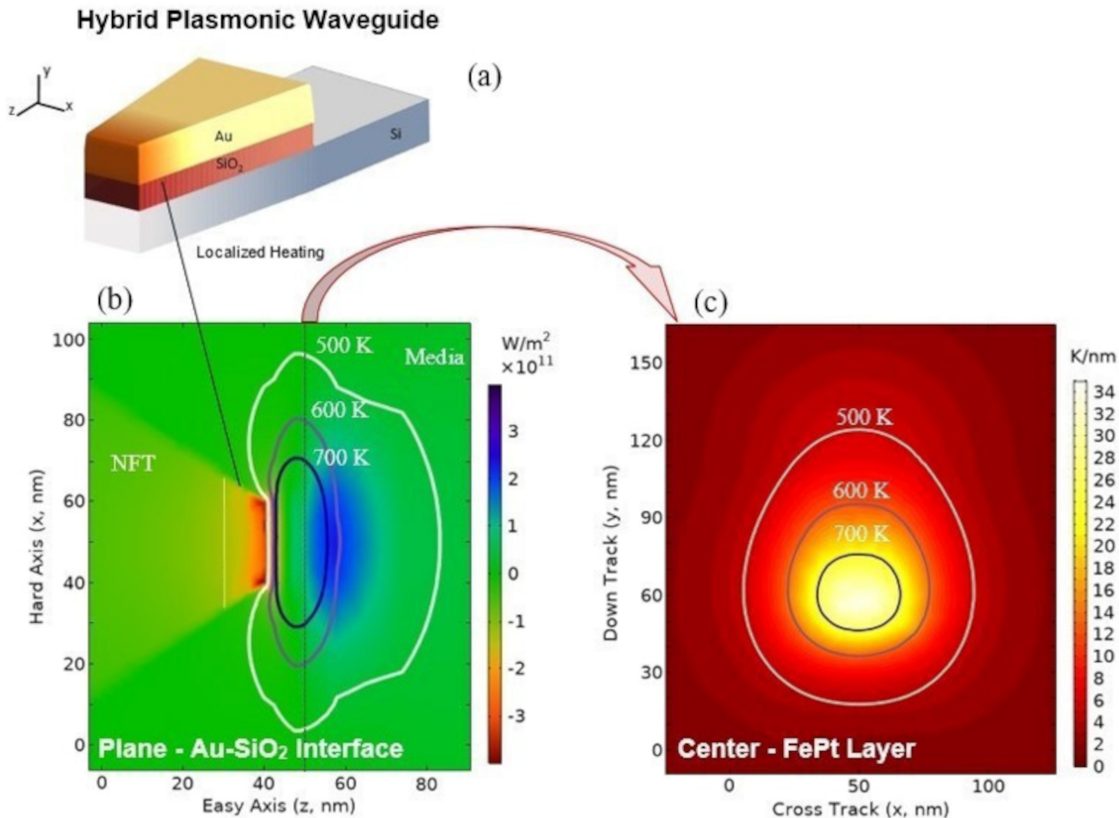


FIG. 4. (a) Minimal model of a M-I-S hybrid plasmonic waveguide suitable as an NFT for HAMR, from Ref. [9]. The air-bearing surface (ABS) is 20 nm along the x-direction (cross track) and 70 nm (Au + SiO₂) in the y-direction (down track). See Supplemental Material [30] for a full list of dimensions. (b) Planar cross-section taken from the metal-insulator interface showing the location of maximum heat flux (W/m²). AuPt/Pd alloys with concentrations of Pd/Pt of 30, 50, or 70% were simulated in the NFT region with highest power per unit area (demarked by white dotted line) where softening of the Au may occur given temperatures circa 400 K. (c) Cross section from the center of the recording layer (black vertical line in (b)) located 13.5 nm away from the ABS, showing temperatures reaching above typical values for the Curie temperature of FePt. The magnitude of the temperature gradient is also plotted with maximum cross- and down-track values listed in Table I.

alloys that have larger thermal conductivities than pure Au are desired. Therefore, Table I reports on a number of Au_xAg_{1-x} alloys used to replace the entire metallic section of the NFT with a noticeable effect. In particular, a crucial figure of merit for thermal stability, which compares the change in FePt temperature to that of the Au in the NFT ($\Delta T_{\text{Media}}/\Delta T_{\text{Au}}$), is markedly improved. It should be noted that thermal gradients in the recording layer, a crucial figure of merit for bit density, tends to be larger for Au alloys that index match well with pure Au and more effectively localize power within the recording layer, i.e., more effectively demonstrate better optical efficiency.

Au alloyed with a small percentage (10%) of Pt/Pd, which are expected to have improved hardness by the rule of mixing, also performed well by demonstrating in simulation a similar figure of merit for thermal stability to that of pure Au. However for alloys with higher concentrations of Pd/Pt, replacing the entire metallic component yielded a lower optical and thermally efficiency in

simulation, due to poorer index matching between photonic and plasmonic modes. However, they were simulated to be potentially suitable for transducer operation when replacing a smaller section near the tip of the NFT where the majority of power is concentrated. Although optical and thermal efficiency was lower, these alloys are anticipated to have smaller coefficients of expansion.

To conclude, we have calculated electronic and thermal material parameters used to measure the plasmonic performance for Au-M alloys suitable for nanoheating applications. By substituting, fully or partially, the metallic parts of a previously-introduced model NFT design, we demonstrate that plasmonic performance is generally maintained or reduced at 830 nm. However, it potentially enables the engineering of desired thermal performance of Au-based NFTs and possibly improved mechanical durability under relatively high-power conditions. We presented the multiscale design protocol as a proof-of-concept within a representative, previously-demonstrated NFT design; however, it is suitable to be

Alloying of metallic section of NFT and heat-sink for optimized nanoheating figures of merit					
	$\Delta T_{\text{FePt}} / \Delta T_{\text{metal}}$	$T_{\text{metal}}^{\text{max}}$ (K)	$T_{\text{FePt}}^{\text{max}}$ (K)	Max. cross. track grad. (K / nm)	Max. down track grad. (K / nm)
(Au), $n \approx 0.068$, $P_{\text{in}} = 3.75$ mW	6.2	389	891	16.7	17.6
(AuAg ₇) $P_{\text{in}} = 4.00$ mW	6.5	381	867	15.3	16.0
(AuAg ₃) $P_{\text{in}} = 6.75$ mW	7.1	376	885	11.7	10.8
(Au _{0.125} Ag _{0.875}) $P_{\text{in}} = 4.50$ mW	7.0	381	911	15.3	15.7
(Au _{0.9} Pd _{0.1}) $P_{\text{in}} = 6.50$ mW	6.2	393	911	11.3	15.4
Alloying 10 nm tip of metallic section					
(Pd) $P_{\text{in}} = 3.75$ mW	3.0	418	668	8.1	9.4
(Au _{0.5} Pd _{0.5}) $P_{\text{in}} = 3.75$ mW	4.5	393 (436 in alloy section)	740	9.8	11.3
(Au _{0.3} Pt _{0.7}) $P_{\text{in}} = 4.25$ mW	4.7	402 (432 in alloy section)	800	10.8	12.5
(Au _{0.7} Pt _{0.3}) $P_{\text{in}} = 4.25$ mW	4.8	393 (402 in alloy section)	775	9.4	11.1

TABLE I. Simulated thermal efficiency of NFT with tapered, hybrid plasmonic waveguide [9] using various Au-alloys. A temperature under 400 K is here considered desirable for Au while maximizing the temperature in the media. High thermal gradients are also here considered desirable in order to localize the heating as much as possible. Reported values for the refractive index of Au vary, and the value used here for Au of $n \approx 0.068$ is derived from first principles.

modified for a number of nanoscale heating applications. Despite our focus on a single operation wavelength and temperature, our assessment procedure is easily applicable to any wavelength and reasonable temperature at which phonon contributions are relatively small.

ACKNOWLEDGMENT

We acknowledge the support of Trinity College Dublin School of Physics, Science Foundation Ireland

(SFI) through The Advanced Materials and Bioengineering Research Centre (AMBER, grant 12/RC/2278, 12/RC/2278.P2 and 15/IA/2854), and the European Regional Development Fund (ERDF) and the EU Horizon 2020 - Marie Skłodowska-Curie grant 713567. We also acknowledge the DJEI/DES/SFI/HEA Irish Centre for High-End Computing (ICHEC) for the provision of computational facilities and support. We further acknowledge Trinity Centre for High Performance Computing and Science Foundation Ireland, for the maintenance and funding, respectively, of the Boyle cluster on which further calculations were performed.

-
- [1] M. Alagiri, P. Rameshkumar, and A. Pandikumar, Gold nanorod-based electrochemical sensing of small biomolecules: A review, *Microchimica Acta* **184**, 3069 (2017).
 - [2] S. Bengali and M. Giri, *Gold sensor* (2018), US Patent App. 15/749,036.
 - [3] M. Rodrigues, D. Costa, R. Domingues, M. Apreutesei, P. Pedrosa, N. Martin, V. Correló, R. Reis, E. Alves, N. Barradas, P. Sampaio, J. Borges, and F. Vaz, Optimization of nanocomposite Au/TiO₂ thin films towards lspr optical-sensing, *Applied Surface Science* **438**, 74 (2018), 10th International Conference on Materials Science & Engineering.
 - [4] P. K. Jain, I. H. El-Sayed, and M. A. El-Sayed, Au nanoparticles target cancer, *Nano Today* **2**, 18 (2007).
 - [5] X. Zhang, Gold nanoparticles: Recent advances in the biomedical applications, *Cell Biochemistry and Biophysics* **72**, 771 (2015).
 - [6] S. Tran, P.-J. DeGiovanni, B. Piel, and P. Rai, Cancer nanomedicine: a review of recent success in drug delivery, *Clinical and Translational Medicine* **6**, 44 (2017).
 - [7] F. Bello, N. Kongsuwan, J. F. Donegan, and O. Hess, Controlled cavity-free, single-photon emission and bipartite entanglement of near-field-excited quantum emitters, *Nano Letters* **20**, 5830 (2020).
 - [8] F. Bello, S. Sanvito, O. Hess, and J. F. Donegan, Shaping and storing magnetic data using pulsed plasmonic nanoheating and spin-transfer torque, *ACS Photonics* **6**, 1524 (2019).
 - [9] C. Black, S. Gates, C. Murray, and S. Sun, *Magnetic storage medium formed of nanoparticles* (2000).
 - [10] M. Mansuripur, A. R. Zakharian, A. Lesuffleur, S.-H. Oh, R. J. Jones, N. C. Lindquist, H. Im, A. Kobayakov, and J. V. Moloney, Plasmonic nano-structures for optical data storage, *Opt. Express* **17**, 14001 (2009).
 - [11] I. Sato, T. Oike, and N. Hanashima, Heat assisted magnetic recording head and heat assisted magnetic record-

- ing apparatus for heating a recording region in a magnetic recording medium during magnetic recording (2009), uS Patent 7,538,978.
- [12] J. Zou, K. Gao, W. Challener, M. Ostrowski, V. Inturi, T. Zhao, and M. Kautzky, [Recording head for heat assisted magnetic recording with diffusion barrier surrounding a near field transducer](#) (2014).
- [13] V. Amendola, R. Pilot, M. Frascioni, O. M. Maragò, and M. A. Iatì, Surface plasmon resonance in gold nanoparticles: a review, [Journal of Physics: Condensed Matter](#) **29**, 203002 (2017).
- [14] N. Bodenschatz, A. Liemert, S. Schnurr, U. Wiedwald, and P. Ziemann, Extending the 3ω method: Thermal conductivity characterization of thin films, [Review of Scientific Instruments](#) **84**, 084904 (2013).
- [15] W. M. Abbott, C. P. Murray, C. Zhong, C. Smith, C. McGuinness, E. Rezvani, C. Downing, D. Daly, A. K. Petford-Long, F. Bello, D. McCloskey, and J. F. Donegan, Less is more: Improved thermal stability and plasmonic response in Au films via the use of subnanometer ti adhesion layers, [ACS Applied Materials & Interfaces](#) **11**, 7607 (2019).
- [16] M. G. Blaber, M. D. Arnold, and M. J. Ford, A review of the optical properties of alloys and intermetallics for plasmonics, [Journal of Physics: Condensed Matter](#) **22**, 143201 (2010).
- [17] B. Dastmalchi, P. Tassin, T. Koschny, and C. M. Soukoulis, A new perspective on plasmonics: Confinement and propagation length of surface plasmons for different materials and geometries, [Advanced Optical Materials](#) **4**, 177 (2016).
- [18] D. Beaglehole and E. Erlbach, Electronic structure of noble-metal-noble-metal alloys, [Phys. Rev. B](#) **6**, 1209 (1972).
- [19] Y. Nishijima, Y. Hashimoto, G. Seniutinas, L. Rosa, and S. Juodkazis, Engineering gold alloys for plasmonics, [Applied Physics A](#) **117**, 641 (2014).
- [20] C. Gong and M. S. Leite, Noble metal alloys for plasmonics, [ACS Photonics](#) **3**, 507 (2016).
- [21] Y. Hashimoto, G. Seniutinas, A. Balčytis, S. Juodkazis, and Y. Nishijima, Au-ag-cu nano-alloys: tailoring of permittivity, [Scientific reports](#) **6** (2016).
- [22] X. X. Anurup Datta, Comparative study of optical near-field transducers for heat-assisted magnetic recording, [Optical Engineering](#) **56**, 1 (2017).
- [16] F. Bello, D. Wolf, G. J. Parker, C. Wolf, A. Krichevsky, F. Zong, N. Abadía, and J. F. Donegan, Optical, thermal, and bit-writing analysis of a directly coupled plasmonic waveguide for heat-assisted magnetic recording, [OSA Continuum](#) **3**, 2010 (2020).
- [9] N. Abadía, F. Bello, C. Zhong, P. Flanigan, D. M. McCloskey, C. Wolf, A. Krichevsky, D. Wolf, F. Zong, A. Samani, D. V. Plant, and J. F. Donegan, Optical and thermal analysis of the light-heat conversion process employing an antenna-based hybrid plasmonic waveguide for hamr, [Opt. Express](#) **26**, 1752 (2018).
- [25] H. Yang, J. Li, and G. Xiao, Decay and propagation properties of symmetric surface plasmon polariton mode in metal-insulator-metal waveguide, [Optics Communications](#) **395**, 159 (2017), nano-Optoelectronics: Advanced Optoelectronic Devices Based on Nanostructures and Nanomaterials.
- [26] C. Sönnichsen, T. Franzl, T. Wilk, G. von Plessen, and J. Feldmann, Plasmon resonances in large noble-metal clusters, [New Journal of Physics](#) **4**, 93 (2002).
- [27] A. J. Haes, S. Zou, G. C. Schatz, and R. P. Van Duyne, A nanoscale optical biosensor: the long range distance dependence of the localized surface plasmon resonance of noble metal nanoparticles, [The Journal of Physical Chemistry B](#) **108**, 109 (2004).
- [28] A. V. Zayats, I. I. Smolyaninov, and A. A. Maradudin, Nano-optics of surface plasmon polaritons, [Physics Reports](#) **408**, 131 (2005).
- [10] C. AB, Comsol multiphysics® v. 5.4, stockholm, Sweden.
- [30] See Supplemental Materials [URL](#), which includes Refs. [n-m].
- [31] V. Krishnamurthy, D. K. T. Ng, K. P. Lim, and Q. Wang, Efficient integrated light-delivery system design for hamr: Maximal optical coupling for transducer and nanowaveguide, [IEEE Transactions on Magnetics](#) **52**, 1 (2016).
- [32] C. Zhong, P. Flanigan, N. Abadía, F. Bello, B. D. Jennings, G. Atcheson, J. Li, J.-Y. Zheng, J. J. Wang, R. Hobbs, D. McCloskey, and J. F. Donegan, Effective heat dissipation in an adiabatic near-field transducer for hamr, [Opt. Express](#) **26**, 18842 (2018).
- [33] H. Boersch, H. Miessner, and W. Raith, Untersuchungen zur winkelabhängigkeit des 14,7 ev-energieverlustes von elektronen in aluminium, [Zeitschrift für Physik](#) **168**, 404 (1962).
- [34] H. Raether, Electron energy loss spectroscopy, Springer Tracts in Modern Physics **38**, 85 (1965).
- [35] H. Froitzheim, Electron energy loss spectroscopy, in [Electron Spectroscopy for Surface Analysis](#), edited by H. Ibach (Springer Berlin Heidelberg, Berlin, Heidelberg, 1977) pp. 205–250.
- [36] R. A. Ferrell, Angular dependence of the characteristic energy loss of electrons passing through metal foils, [Phys. Rev.](#) **101**, 554 (1956).
- [37] D. Bohm and D. Pines, A collective description of electron interactions. i. magnetic interactions, [Phys. Rev.](#) **82**, 625 (1951).
- [38] D. Pines and D. Bohm, A collective description of electron interactions: Ii. collective vs individual particle aspects of the interactions, [Phys. Rev.](#) **85**, 338 (1952).
- [39] D. Bohm and D. Pines, A collective description of electron interactions: Iii. coulomb interactions in a degenerate electron gas, [Phys. Rev.](#) **92**, 609 (1953).
- [40] M. Rocca, Low-energy eels investigation of surface electronic excitations on metals, [Surface Science Reports](#) **22**, 1 (1995).
- [41] M. G. Blaber, M. D. Arnold, and M. J. Ford, A review of the optical properties of alloys and intermetallics for plasmonics, [Journal of Physics: Condensed Matter](#) **22**, 143201 (2010).
- [6] O. K. Orhan and D. D. O'Regan, Plasmonic performance of $\text{Au}_x\text{Ag}_y\text{Cu}_{1-x-y}$ alloys from many-body perturbation theory, [Journal of Physics: Condensed Matter](#) **31**, 315901 (2019).
- [43] P. Hohenberg and W. Kohn, Inhomogeneous electron gas, [Phys. Rev.](#) **136**, B864 (1964).
- [44] W. Kohn and L. J. Sham, Self-consistent equations including exchange and correlation effects, [Phys. Rev.](#) **140**, A1133 (1965).
- [45] D. C. Langreth and J. P. Perdew, Theory of nonuniform electronic systems. i. analysis of the gradient approximation and a generalization that works, [Phys. Rev. B](#) **21**, 5469 (1980).

- [46] J. P. Perdew, Density-functional approximation for the correlation energy of the inhomogeneous electron gas, *Phys. Rev. B* **33**, 8822 (1986).
- [47] J. P. Perdew, J. A. Chevary, S. H. Vosko, K. A. Jackson, M. R. Pederson, D. J. Singh, and C. Fiolhais, Atoms, molecules, solids, and surfaces: Applications of the generalized gradient approximation for exchange and correlation, *Phys. Rev. B* **46**, 6671 (1992).
- [48] A. D. McLachlan and M. A. Ball, Time-dependent hartree-fock theory for molecules, *Rev. Mod. Phys.* **36**, 844 (1964).
- [49] T. Rangel, D. Kecik, P. E. Trevisanutto, G.-M. Rignanese, H. Van Swygenhoven, and V. Olevano, Band structure of gold from many-body perturbation theory, *Phys. Rev. B* **86**, 125125 (2012).
- [50] H. Eckardt, L. Fritsche, and J. Noffke, Self-consistent relativistic band structure of the noble metals, *Journal of Physics F: Metal Physics* **14**, 97 (1984).
- [51] A. J. Cohen, P. Mori-Sánchez, and W. Yang, Challenges for density functional theory, *Chemical Reviews* **112**, 289 (2012), <http://dx.doi.org/10.1021/cr200107z>.
- [52] A. Marini, G. Onida, and R. Del Sole, Quasiparticle electronic structure of copper in the *GW* approximation, *Phys. Rev. Lett.* **88**, 016403 (2001).
- [53] A. Marini, R. Del Sole, and G. Onida, First-principles calculation of the plasmon resonance and of the reflectance spectrum of silver in the *GW* approximation, *Phys. Rev. B* **66**, 115101 (2002).
- [54] A. Marini, R. Del Sole, A. Rubio, and G. Onida, Quasiparticle band-structure effects on the d hole lifetimes of copper within the *gw* approximation, *Phys. Rev. B* **66**, 161104 (2002).
- [8] A. Marini, C. Hogan, M. Grüning, and D. Varsano, yambo: An ab initio tool for excited state calculations, *Computer Physics Communications* **180**, 1392 (2009).
- [56] A. Marini, *Optical and electronic properties of Copper and Silver: from Density Functional Theory to Many Body Effects*, Ph.D. thesis, PhD Dissertation, University of Rome-Tor Vergata (2001).
- [57] P. Drude, Zur elektronentheorie der metalle, *Annalen der Physik* **306**, 566 (1900).
- [58] P. Drude, Zur elektronentheorie der metalle; ii. teil. galvanomagnetische und thermomagnetische effecte, *Annalen der Physik* **308**, 369 (1900).
- [59] H. A. Lorentz, *The Theory of Electrons and Its Applications to the Phenomena of Light and Radiant Heat: A Course of Lectures Delivered in Columbia University, New York, in March and April, 1906*, Vol. 29 (Columbia University Press, 1909).
- [60] M. Fox, *Optical properties of solids*, Vol. 3 (Oxford university press, 2010).
- [61] R. T. Beach and R. W. Christy, Electron-electron scattering in the intraband optical conductivity of cu, ag, and au, *Phys. Rev. B* **16**, 5277 (1977).
- [62] M. H. Cohen, Optical constants, heat capacity and the fermi surface, *The Philosophical Magazine: A Journal of Theoretical Experimental and Applied Physics* **3**, 762 (1958), <https://doi.org/10.1080/14786435808237011>.
- [63] H. Okamoto and T. B. Massalski, The Ag-Au (silver-gold) system, *Bulletin of Alloy Phase Diagrams* **4**, 30 (1983).
- [64] H. Okamoto, D. J. Chakrabarti, D. E. Laughlin, and T. B. Massalski, The Au-Cu (gold-copper) system, *Journal of Phase Equilibria* **8**, 454 (1987).
- [65] H. Okamoto and T. B. Massalski, The Au-Pd (gold-palladium) system, *Bulletin of Alloy Phase Diagrams* **6**, 229 (1985).
- [66] H. Okamoto and T. B. Massalski, The Au-Pt (gold-platinum) system, *Bulletin of Alloy Phase Diagrams* **6**, 46 (1985).
- [67] L. Nordheim, Zur elektronentheorie der metalle. i, *Annalen der Physik* **401**, 607.
- [68] L. Bellaiche and D. Vanderbilt, Virtual crystal approximation revisited: Application to dielectric and piezoelectric properties of perovskites, *Phys. Rev. B* **61**, 7877 (2000).
- [69] F. Bello, O. K. Orhan, N. Abadía, D. D. O'Regan, and J. F. Donegan, Material characterization and thermal performance of Au alloys in a thin-film plasmonic waveguide, in *Conference on Lasers and Electro-Optics* (Optical Society of America, 2019) p. JTu2A.110.

**SUPPLEMENTAL MATERIAL FOR
“MULTISCALE DESIGN OF AU-BASED ALLOYS
FOR IMPROVED PLASMON DELIVERY AND
NANOHEATING IN NEAR-FIELD
TRANSDUCERS”**

I. COMPUTATIONAL METHODOLOGY

The initial crystallographic information for bulk Au, Ag, Cu were adopted from Ref. 1, and for bulk Pd, and Pt from Ref. 2. Bespoke, norm-conserving PBE pseudo-potentials for the elemental metals were produced using the pseudo-potential generator OPIUM [3], and the pre-processing tool within Quantum ESPRESSO software [4, 5] was used to produce the VCA pseudo-potentials. The approximate KS electronic structures were obtained by performing full-geometry optimization, self-consistent field (SCF) and non-self-consistent field (NSCF) simulations, in order, using the Quantum ESPRESSO software with the converged parameters used from Ref. 6, as well as the choice of smearing parameter for the Marzari-Vanderbilt cold smearing [7], namely 0.1 eV. The G_0W_0 and spectral simulations for the inter-band contributions were performed using the Yambo code [8].

The Fermi velocities, and Drude plasmon energies were evaluated using an in-house post-processing code starting from the KS band-structures [6]. For finite-element simulations, we have used scattering boundary conditions within the COMSOL Multiphysics modeling software for the outer boundaries of the cladding material (SiO_2) [9, 10]. The medium had a simulated in-plane area of $450 \times 750 \text{ nm}^2$. Any resistive heating beyond this region was determined to have negligible impact on the area of maximum heating. FEM simulations used a minimum element size of 4.2 nm, maximum growth rate of 1.4, and curvature factor of 0.4 for convergence of results. We have only reported on the most optimal Au-based alloys identified in simulation for nanoscale heating with a specific antenna-based, plasmonic NFT.

**II. SEMI-EMPIRICAL THERMAL
PARAMETERS**

The thermal conductivity of metals is quite a complicated quantity, to which various scattering processes such as the electron-phonon, the electron-electron, as well as the electron-impurity scattering all contribute in the case of the noble metals and their alloys up to their melting points [11]. The electrical thermal conductivity, κ_e , is related to the electrical conductivity, σ , via the Wiedermann-Franz law [12] given by

$$\kappa_e = \frac{3}{2} \left(\frac{k_B}{e} \right)^2 T \sigma, \quad (1)$$

where k_B and T are the Boltzmann constant and temperature, respectively. The electrical conductivity can be described within the Drude theory, which was used in Ref. 6 to approximate the phenomenological plasmon life-times, τ_p , per

$$\sigma = \frac{n_c e^2 \tau_p}{m_{\text{eff}}}, \quad (2)$$

where n_c is the carrier density, which is the density of state at the Fermi level, $N(E_F)$, per unit volume. The effective mass, m_{eff} can be approximated using the Fermi velocity, within the one-band theory assuming that the electronic bands have parabolic dispersion, by $m_{\text{eff}}^{-1} \approx \langle v^2(E_F) \rangle$. Then, the electronic thermal conductivity is given by

$$\kappa_e = \frac{3}{2} k_B^2 T \frac{N(E_F)}{V_{\text{cell}}} \langle v^2(E_F) \rangle \tau_p. \quad (3)$$

For $\text{Au}_x\text{M}_{1-x}$ alloys Eq. 3 is reduces to

$$\kappa_e(x) = [x f_{\text{Au}} + (1-x) f_{\text{M}}] T \frac{N(E_F)}{V_{\text{cell}}} \langle v^2(E_F) \rangle, \quad (4)$$

where the scaling factor f_M for the given elemental metal M is obtained from

$$f_M = \frac{\kappa_{\text{exp}}^{\text{M}}(T)}{T} \frac{V_{\text{cell}}}{N(E_F) \langle v^2(E_F) \rangle}, \quad (5)$$

using the experimental thermal conductivity values at 400 K for elemental metals shown below.

	Au [13]	Ag [13]	Cu [13]	Pd [14]	Pt [15]
$\kappa_{\text{exp}}^{\text{M}}$	312	420	392	75	72
$T = 400 \text{ K}$					

TABLE I. Experimental thermal conductivity for the elemental metals at $T = 400 \text{ K}$ used to determine the scaling parameters for alloys.

The specific heat due to charge carriers is calculated using first-principles electronic parameters derived via the Drude definition of the electronic heat capacity per unit volume, c_e , at low temperature, given by [11]

$$C_e = \frac{\pi^2}{3} N(E_F) E_F k_B \frac{T}{T_F}, \quad (6)$$

where $T_F = E_F/k_B$ and E_F is the Fermi energy. Then the electronic specific heat can be expressed as

$$c_e = \frac{\pi^2}{3 m_{\text{avr}}} N(E_F) k_B^2 T, \quad (7)$$

where m_{avr} is the averaged atomic mass for the $\text{Au}_x\text{M}_{1-x}$ given by

$$m_{\text{avr}} = x m_{\text{Au}} + (1-x) m_{\text{M}}. \quad (8)$$

III. OPTIMIZED FIRST-PRINCIPLES SIMULATION PARAMETERS

Level	Parameter	Value
GeoOpt	The plane-wave kinetic energy cutoff energies	75 Ry
	k-points	$4 \times 4 \times 4$
	The plane-wave kinetic energy cutoff energies	25 Ry
SCF	k-points	$21 \times 21 \times 21$
	The plane-wave kinetic energy cutoff energies	25 Ry
NSCF	k-points	$16 \times 16 \times 16$
	Number of bands	100
	Number of bands in the self-energy exchange	10
G ₀ W ₀	Number of bands in the self-energy correlation	100

TABLE II. The converged parameters used in the geometry optimization (GeoOpt), self-consistent field (SCF), non-self-consistent field (NSCF), and G₀W₀.

IV. THERMAL AND OPTICAL PARAMETERS

System	κ (W m ⁻¹ K ⁻¹)	c_e ($\times 10^{-3}$ J gm ⁻¹ K ⁻¹)	n	k
Au	312.0	0.273	0.068	5.176
Au ₇ Ag	271.2	0.297	0.148	5.454
Au ₃ Ag	600.0	0.326	0.115	8.133
AuAg	467.2	0.329	0.071	6.467
AuAg ₃	669.2	0.417	0.091	8.034
AuAg ₇	347.9	0.452	0.054	5.485
Ag	420.0	0.459	0.045	5.675

TABLE III. The thermal conductivity (κ), and the electronic specific heat (c_e) at 400 K; the refractive index (n), and the extinction coefficient (k) at 830 nm of the mono-layer-stacked ordered Au-Ag alloys for available stoichiometric ratios.

System	κ (W m ⁻¹ K ⁻¹)	c_e ($\times 10^{-3}$ J gm ⁻¹ K ⁻¹)	n	k
Au	312.0	0.273	0.068	5.176
Au _{0.875} Ag _{0.125}	340.9	0.265	0.077	5.207
Au _{0.75} Ag _{0.25}	365.0	0.281	0.072	5.342
Au _{0.5} Ag _{0.5}	390.1	0.306	0.057	5.545
Au _{0.25} Ag _{0.75}	465.7	0.388	0.057	6.067
Au _{0.125} Ag _{0.875}	469.0	0.413	0.053	6.096
Ag	420.0	0.459	0.045	5.675

TABLE IV. The thermal conductivity (κ), and the electronic specific heat (c_e) at 400 K; the refractive index (n), and the extinction coefficient (k) at 830 nm of the disordered Au_xAg_{1-x} alloys for available stoichiometric ratios.

System	κ (W m ⁻¹ K ⁻¹)	c_e ($\times 10^{-3}$ J gm ⁻¹ K ⁻¹)	n	k
Au	312.0	0.273	0.068	5.176
Au ₇ Cu	253.9	0.329	0.159	5.295
Au ₃ Cu	591.1	0.373	0.140	8.194
AuCu	451.3	0.570	0.110	6.629
AuCu ₃	586.7	0.775	0.134	7.732
AuCu ₇	278.9	0.939	0.123	4.969
Cu	392.0	1.199	0.080	5.397

TABLE V. The thermal conductivity (κ), and the electronic specific heat (c_e) at 400 K; the refractive index (n), and the extinction coefficient (k) at 830 nm of the mono-layer-stacked ordered Au-Cu alloys for available stoichiometric ratios.

System	κ (W m ⁻¹ K ⁻¹)	c_e ($\times 10^{-3}$ J gm ⁻¹ K ⁻¹)	n	k
Au	312.0	0.273	0.068	5.176
Au _{0.875} Cu _{0.125}	341.4	0.313	0.094	5.227
Au _{0.75} Cu _{0.25}	365.6	0.386	0.109	5.186
Au _{0.5} Cu _{0.5}	387.8	0.572	0.128	5.480
Au _{0.25} Cu _{0.75}	395.0	0.858	0.129	5.327
Au _{0.125} Cu _{0.875}	379.2	1.012	0.130	4.916
Cu	392.0	1.199	0.080	5.397

TABLE VI. The thermal conductivity (κ), and the electronic specific heat (c_e) at 400 K; the refractive index (n), and the extinction coefficient (k) at 830 nm of the disordered Au_xCu_{1-x} alloys for available stoichiometric ratios.

System	κ	c_e	n	k
	(W m ⁻¹ K ⁻¹)	($\times 10^{-3}$ J gm ⁻¹ K ⁻¹)		
Au	312.0	0.273	0.068	5.176
Au _{0.9} Pd _{0.1}	488.5	0.330	0.098	7.560
Au _{0.8} Pd _{0.2}	265.9	0.219	0.173	6.632
Au _{0.7} Pd _{0.3}	619.4	0.611	0.500	8.861
Au _{0.6} Pd _{0.4}	468.8	0.479	0.518	7.675
Au _{0.5} Pd _{0.5}	143.7	0.949	1.274	5.505
Au _{0.4} Pd _{0.6}	211.1	1.997	1.275	6.113
Au _{0.3} Pd _{0.7}	220.7	2.437	1.131	6.942
Au _{0.2} Pd _{0.8}	204.8	2.838	1.137	7.120
Au _{0.1} Pd _{0.9}	179.3	3.364	1.219	7.115
Pd	75.0	4.812	1.544	3.954

TABLE VII. The thermal conductivity (κ), and the electronic specific heat (c_e) at 400 K; the refractive index (n), and the extinction coefficient (k) at 830 nm of the disordered Au_xPd_{1-x} alloys for available stoichiometric ratios.

System	κ	c_e	n	k
	(W m ⁻¹ K ⁻¹)	($\times 10^{-3}$ J gm ⁻¹ K ⁻¹)		
Au	312.0	0.273	0.068	5.176
Au _{0.9} Pt _{0.1}	493.5	0.329	0.101	7.385
Au _{0.8} Pt _{0.2}	303.2	0.261	0.670	6.879
Au _{0.7} Pt _{0.3}	602.0	0.586	0.908	9.027
Au _{0.6} Pt _{0.4}	477.6	0.529	0.957	8.721
Au _{0.5} Pt _{0.5}	143.3	0.670	1.177	5.571
Au _{0.4} Pt _{0.6}	183.5	1.030	1.091	6.565
Au _{0.3} Pt _{0.7}	179.1	1.374	1.211	6.448
Au _{0.2} Pt _{0.8}	184.1	1.696	1.033	7.029
Au _{0.1} Pt _{0.9}	127.4	2.110	1.815	5.382
Pt	72.0	2.150	1.363	5.406

TABLE VIII. The thermal conductivity (κ), and the electronic specific heat (c_e) at 400 K; the refractive index (n), and the extinction coefficient (k) at 830 nm of the disordered Au_xPt_{1-x} alloys for available stoichiometric ratios.

V. FINITE-ELEMENT SIMULATION PARAMETERS

Waveguide dimensions	
Si waveguide length, width (x)	0.5 μ m, 450 nm
Si waveguide thickness (y)	250 nm
Au film thickness	60 nm
Taper /Au/SiO ₂ /Si length (z)	330 nm
Au, SiO ₂ , Si tip width	20 nm
SiO ₂ thickness	10 nm
Heat-sink (Au) length, width	222 nm, 450 nm
Heat-sink thickness	150 nm
Write pole length, width	50 nm, 450 nm
Write pole thickness	100 nm

TABLE IX. Dimensions from Refs. [9, 16] of the photonic and plasmonic waveguide design used as an example in simulations.

Film				
	Thickness (nm)	n $\lambda = 830 \text{ nm}$	C ($\times 10^6 \text{ J m}^{-3} \text{ K}^{-1}$)	κ ($\text{W m}^{-1} \text{ K}^{-1}$)
Heated air/lubricant	2.5	1.0	1.0	3.0
Carbon overcoat	6.5	$2.4+0.51i$	1.0	1.0
Capping	1.5 nm	$4.71+3.38i$	2.89	20.0
FePt	9	$3.04+2.69i$	2.89	5.7, 1.4 (in-plane)
MgO	7	1.65	3.36	30.0
Amorphous underlayer	9	$5.87+4.68i$	1.1	50.0
Heat-sink	72	$3.72+3.99i$	3.06	10.5
Materials (NFT, waveguide)				
Au		$0.16+5.15i$	2.49	317
SiO ₂	1.45	1.6	1.4	
Si		3.67	1.63	131
Write pole		$2.14+4.24i$	3.73	3.0

TABLE X. Film thickness, refractive index (n) at 830 nm, specific heat capacity (C), and electronic thermal conductivity (κ) values from Refs. [9, 16], used here as an example for finite-element simulations.

- [1] I.-K. Suh, H. Ohta, and Y. Waseda, High-temperature thermal expansion of six metallic elements measured by dilatation method and x-ray diffraction, *Journal of Materials Science* **23**, 757 (1988).
- [2] J. Zemmann, Crystal structures, 2nd edition. vol. 1 by r. w. g. wyckoff, *Acta Crystallographica* **18**, 139 (1965).
- [3] Opium:the optimized pseudopotential interface unification module, <http://opium.sourceforge.net/>, accessed: 2017-11-30.
- [4] P. Giannozzi, S. Baroni, N. Bonini, M. Calandra, R. Car, C. Cavazzoni, D. Ceresoli, G. L. Chiarotti, M. Cococcioni, I. Dabo, A. D. Corso, S. de Gironcoli, S. Fabris, G. Fratesi, R. Gebauer, U. Gerstmann, C. Gougoussis, A. Kokalj, M. Lazzeri, L. Martin-Samos, N. Marzari, F. Mauri, R. Mazzarello, S. Paolini, A. Pasquarello, L. Paulatto, C. Sbraccia, S. Scandolo, G. Sclauzero, A. P. Seitsonen, A. Smogunov, P. Umari, and R. M. Wentzcovitch, Quantum espresso: a modular and open-source software project for quantum simulations of materials, *Journal of Physics: Condensed Matter* **21**, 395502 (2009).
- [5] P. Giannozzi, O. Andreussi, T. Brumme, O. Bunau, M. B. Nardelli, M. Calandra, R. Car, C. Cavazzoni, D. Ceresoli, M. Cococcioni, N. Colonna, I. Carnimeo, A. D. Corso, S. de Gironcoli, P. Delugas, R. A. D. Jr, A. Ferretti, A. Floris, G. Fratesi, G. Fugallo, R. Gebauer, U. Gerstmann, F. Giustino, T. Gorni, J. Jia, M. Kawamura, H.-Y. Ko, A. Kokalj, E. Küçükbenli, M. Lazzeri, M. Marsili, N. Marzari, F. Mauri, N. L. Nguyen, H.-V. Nguyen, A. O. de-la Roza, L. Paulatto, S. Poncé, D. Rocca, R. Sabatini, B. Santra, M. Schlipf, A. P. Seitsonen, A. Smogunov, I. Timrov, T. Thonhauser, P. Umari, N. Vast, X. Wu, and S. Baroni, Advanced capabilities for materials modelling with quantum espresso, *Journal of Physics: Condensed Matter* **29**, 465901 (2017).
- [6] O. K. Orhan and D. D. O'Regan, Plasmonic performance of Au_xAg_yCu_{1-x-y} alloys from many-body perturbation theory, *Journal of Physics: Condensed Matter* **31**, 315901 (2019).
- [7] N. Marzari, D. Vanderbilt, A. De Vita, and M. C. Payne, Thermal contraction and disordering of the al(110) surface, *Phys. Rev. Lett.* **82**, 3296 (1999).
- [8] A. Marini, C. Hogan, M. Grüning, and D. Varsano, yambo: An ab initio tool for excited state calculations, *Computer Physics Communications* **180**, 1392 (2009).
- [9] N. Abadía, F. Bello, C. Zhong, P. Flanigan, D. M. McCloskey, C. Wolf, A. Krichevsky, D. Wolf, F. Zong, A. Samani, D. V. Plant, and J. F. Donegan, Optical and thermal analysis of the light-heat conversion process employing an antenna-based hybrid plasmonic waveguide for hamr, *Opt. Express* **26**, 1752 (2018).
- [10] C. AB, *Comsol multiphysics® v. 5.4*, stockholm, Sweden.
- [11] C. Uher, Thermal conductivity of metals, in *Thermal Conductivity: Theory, Properties, and Applications*, edited by T. M. Tritt (Springer US, Boston, MA, 2004) pp. 21–91.
- [12] R. Franz and G. Wiedemann, Ueber die wärmeleitfähigkeit der metalle, *Annalen der Physik* **165**, 497 (1853).
- [13] Y. S. Touloukian, R. W. Powell, C. Y. Ho, and P. G. Klemens, *Thermophysical properties of matter - the TPRC data series. Volume 1. Thermal conductivity - metallic elements and alloys. (Reannouncement)*. Data book, Tech. Rep. (United States, 1970).
- [14] E. M. Savitskii and A. Prince, *Handbook of precious metals* (Hemisphere Publishing Corporation, New York, 1989).
- [15] R. W. Powell, C. Y. Ho, P. E. Liley, U. States., N. B. o. Standards., and D. o. Commerce., *Thermal conductivity of selected materials* (U.S. Dept. of Commerce, National

Bureau of Standards; for sale by the Superintendent of Documents, U.S. Govt. Print. Off., Washington, 1966).

[16] F. Bello, D. Wolf, G. J. Parker, C. Wolf, A. Krichevsky, F. Zong, N. Abadía, and J. F. Donegan, Optical, ther-

mal, and bit-writing analysis of a directly coupled plasmonic waveguide for heat-assisted magnetic recording, [OSA Continuum](#) **3**, 2010 (2020).